

Article

Modification of Cellulose by Esterification Crosslinking to Manipulate Its Microstructure for Enhanced Sodium Storage in Hard Carbon

Xingyun Zhang ^{1,2,†}, Yue Hu ^{2,†}, Yan Wang ², Ming Li ^{3,4}, Cuiying Lu ³, Shixiong Sun ^{2,*} and Junwei Lang ^{1,2,4,*}

¹ Shandong Laboratory of Advanced Materials and Green Manufacturing at Yantai, Yantai 264000, China

² Research Center of Resource Chemistry and Energy Materials, State Key Laboratory of Solid Lubrication, Lanzhou Institute of Chemical Physics, Chinese Academy of Sciences, Lanzhou 730000, China

³ School of Energy Engineering, School of Chemistry and Chemical Engineering, Yulin University, Yulin 719000, China

⁴ Yulin Innovation Institute of Clean Energy, Yulin 719099, China

* Correspondence: hust_sunshixiong@163.com (S.S.); jwlang@licp.acas.cn (J.L.)

† These authors contributed equally to this work.

Abstract: The active hydroxyl group of cellulose plays a crucial role in regulating the microstructure of cellulose-derived hard carbon, which ultimately affects its sodium storage capacity. Through small-angle X-ray scattering (SAXS) and X-ray atomic pair distribution function (PDF) analysis, we proved that modification of cellulose by esterification crosslinking can introduce more closed pores into the carbonized hard carbon, which is beneficial for promoting sodium ion storage. Our results demonstrate that by optimizing the conditions used for esterification cross-linking modification, the sodium storage capacity of cellulose-derived hard carbon could be increased from 254 to 348 mAh g⁻¹, with an increase in plateau capacity from 140 to 230 mAh g⁻¹. This study makes a significant contribution towards establishing industrial applications for cellulose-derived hard carbon.



Academic Editor: Yong-Joon Park

Received: 13 December 2024

Revised: 9 January 2025

Accepted: 13 January 2025

Published: 20 January 2025

Citation: Zhang, X.; Hu, Y.; Wang, Y.; Li, M.; Lu, C.; Sun, S.; Lang, J. Modification of Cellulose by Esterification Crosslinking to Manipulate Its Microstructure for Enhanced Sodium Storage in Hard Carbon. *Batteries* **2025**, *11*, 36. <https://doi.org/10.3390/batteries11010036>

Copyright: © 2025 by the authors. Licensee MDPI, Basel, Switzerland. This article is an open access article distributed under the terms and conditions of the Creative Commons Attribution (CC BY) license (<https://creativecommons.org/licenses/by/4.0/>).

1. Introduction

With energy issues becoming increasingly pressing in modern society, energy conservation and the practical application of energy-storage technology are the next goals in the development of new energy technologies [1,2]. Sodium-ion batteries have emerged as the most suitable battery system for large-scale energy storage, following lithium-ion batteries, due to their potential advantages in terms of resource cost and safety [3,4]. Among the reported electrode materials used for sodium-ion batteries, hard carbon is widely regarded as the preferred anode material owing to its exceptional reversible capacity, favorable electronic conductivity, stable operating potential, and prolonged cycle life, as well as to the abundance of relevant resources [5–8].

Hard carbon can be easily obtained through the carbonization of various organic carbonaceous materials such as banana peels, pomelo peels, coconut shells, peanut shells, wood, bamboo, asphalt, and petroleum coke. It exhibits a specific capacity ranging from 200 to 300 mAh g⁻¹, and has an initial coulombic efficiency below 70% [9–11]. Nevertheless, the practical application of these hard carbons on a large scale remains challenging due to their relatively limited capacity and low initial coulombic efficiency [5]. Therefore, the development of hard carbon materials exhibiting high sodium storage capacity and

high initial coulombic efficiency has emerged as a prominent research focus within the industry [6,8,12]. As is widely acknowledged, hard carbon consists of two distinctive domains: stacked nanometer-scale bent carbon sheets and closing micropores that originate from the interstitial spaces within the nanometer-scale bent carbon sheets [13,14]. Although the amorphous structure of hard carbon poses challenges to investigating its mechanism of sodium storage, current research suggests that enhancing the number of closed pores can effectively enhance the sodium storage capacity of hard carbon [12,15–19]. On the other hand, the initial Coulombic efficiency is a pivotal metric for assessing the performance of hard carbon and is intricately linked to its specific surface area [5]. The initial coulombic efficiency of hard carbon can be effectively enhanced through the reduction of its specific surface area [20].

Therefore, the sodium storage performance of hard carbons can be effectively enhanced through the following strategies: (1) expanding the interlayer of bent carbon sheets in hard carbons [21–23], (2) decreasing the surface area of hard carbons [5,24], and (3) increasing the number of closing micropores in hard carbons [12,14,18,25,26]. Given the aforementioned strategies, a streamlined yet efficacious combination of them would constitute a robust approach to developing a high-capacity hard carbon.

In this work, we selected cellulose as the primary precursor for the synthesis of hard carbon materials due to its high availability, cost-effectiveness, and easily modifiable single-component nature. By employing esterification crosslinking to alter the surface molecular structure of cellulose, we successfully synthesized a diverse range of surface-modified celluloses and achieved the production of nano-structural modified hard carbons through carbonization. Through small-angle X-ray scattering (SAXS) and X-ray atomic pair distribution function (PDF) analysis, we proved that modification of cellulose by esterification crosslinking can introduce more closed pores into the carbonized hard carbon, which is beneficial for promoting sodium ion storage. By optimizing the conditions for esterification crosslinking, we successfully enhanced the sodium storage capacity of cellulose-derived hard carbon from 254 to 348 mAh g^{-1} and achieved an applicable initial coulomb efficiency (ICE) exceeding 85% at a current density of 10 mA g^{-1} , surpassing the performance of currently available commercialized hard carbon products. This breakthrough has significant potential for industrial application.

2. Materials and Methods

Chemical and materials: All chemicals and solutions used were of analytical-grade purity and were purchased from Fuyu Fine Chemical.

Preparation of HC-1: Cellulose was utilized as the direct raw material. It was preheated at 300 °C under Ar gas protection for 2 h, then carbonized at 1300 °C for an additional period of 2 h. Subsequently, the sample was cooled down using furnace cooling to obtain HC-1.

Preparation of HC-2: The process of preparing HC-2 involved a pre-crosslinking treatment on cellulose, in addition to the method employed in HC-1 preparation. The cellulose and terephthalic acid were mixed in a weight ratio of 9:1, and this step was followed by an esterification reaction at 90 °C for 5 h in an electric oven to achieve effective crosslinking between cellulose and terephthalic acid. After the completion of the esterification reaction, the mixture was preheated at 300 °C for 2 h and then subjected to high-temperature carbonization at 1300 °C for another two hours, resulting in the synthesis of the high-performance hard carbon material HC-2.

Preparation of HC-3: In the preparation of HC-3, urea was introduced as a cross-linking catalyst to enhance the degree of cellulose esterification. A uniform composite material was pre-formed by gradually spraying 10 mL of a 2 mol/L urea solution into 100 g of cellulose with continuous stirring to ensure thorough mixing, and this step was

followed by removal of excess moisture through drying at 120 °C and subsequent mixing with terephthalic acid in a weight ratio of 9:1. Effective esterification cross-linking between cellulose and terephthalic acid with the aid of urea as a catalyst was achieved through an esterification reaction at 90 °C for up to 5 h. After the catalytic esterification reaction was complete, a pre-carbonization treatment was conducted at 300 °C under an Ar atmosphere for two hours, and this step was followed by carbonization treatment at a high temperature (1300 °C) for another two hours. This process successfully yielded HC-3.

Composition and structural characterization: The physical structures of the prepared samples were characterized using a Bruker X-ray diffractometer manufactured in Germany. Cu target K α radiation with a wavelength of 0.15405 nm was employed, and the scanning speed was set at 10°/min with a scanning range of $2\theta = 10\text{--}100^\circ$. Fourier transform infrared spectroscopy (FTIR) was performed using a VERTEX 70 spectrometer manufactured by Bruker. The spectroscopy was conducted using a Lab RAM HR Evolution Raman spectrometer (Horiba Jobin Yvon). The surface morphology in this study was examined using scanning electron microscopy (SEM, JSM-6701F, JEOL), and for precise imaging, the high-resolution transmission electron microscopy technique (HRTEM, JEM-2100F) was utilized. The specific surface area was determined by the Brunauer–Emmett–Teller method using a Autosorb-iQ-MP instrument. Thermogravimetric analysis (TGA, Nestal STA449F3) was conducted under an N₂ atmosphere at a heating rate of 5 °C min⁻¹ from room temperature to 1000 °C.

Electrochemical test of anode materials: The active material (80 wt%), the conductive agent acetylene black (10 wt%), and the binder polyvinylidene fluoride (PVDF, 10 wt%) were homogeneously mixed with N-methyl-2-pyrrolidone (NMP) to form a uniform slurry. Subsequently, the slurry was uniformly coated onto copper foil, which was then placed in a vacuum oven and dried at 110 °C for 12 h to eliminate the solvent. Following this step, it was naturally cooled to room temperature. Finally, circular electrodes with a diameter of 12 mm were prepared by cutting using a manual punching machine for battery assembly. The battery assembly was conducted within an argon-filled “MIKROUNA” glove box, ensuring a dry and anaerobic environment with water and oxygen content below 0.01 ppm. The CR2032 battery shell served as the container, while metal sodium sheets were utilized as electrodes. Glass fiber acted as the separator material, and a 1:1 volume ratio solution of diethyl carbonate (DEC) and ethylene carbonate (EC) containing a 1.0 mol L⁻¹ NaClO₄ solution functioned as the electrolyte. The galvanostatic charge–discharge (GCD) measurements were performed on a LAND-2001A battery cycler at 25 °C within the potential range of 0–2 V. Cyclic voltammetry (CV) measurements were conducted using the CHI electrochemical workstation.

3. Results

Figure 1 shows the schematic synthetic pathway of cellulose-derived hard carbons. The cellulose molecule, a polysaccharide composed of glucose units, can undergo direct carbonization to yield a structurally rough and porous form of hard carbon (HC-1). Esterified cellulose (E-cellulose) can be obtained by conducting esterification crosslinking of cellulose with terephthalic acid. Subsequent carbonization of the E-cellulose yielded smooth-surfaced hard carbon (HC-2). In the process of preparing E-cellulose, urea was incorporated as a catalyst to enhance the degree of crosslinking in E-cellulose, thereby yielding catalytic E-cellulose (CE-cellulose). Subsequent carbonization of CE-cellulose yielded hard carbon (HC-3) with a smoother surface. To verify the crosslinking of ester groups, FT-IR analysis was performed. As shown in Figure 2a, besides the characteristic absorption peaks of the cellulose, a new peak near 1720 cm⁻¹ was observed in E-cellulose and CE-cellulose, indicating the presence of an ester bond (C=O) stretching vibration.

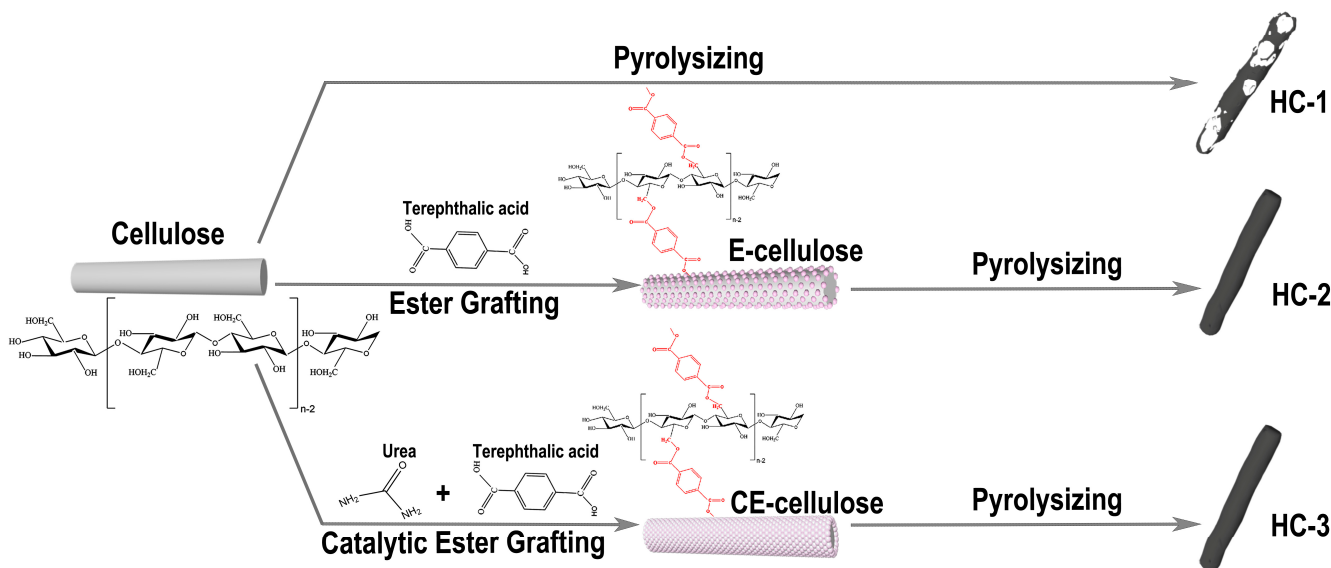


Figure 1. Schematic of the synthetic pathway of cellulose-derived hard carbon.

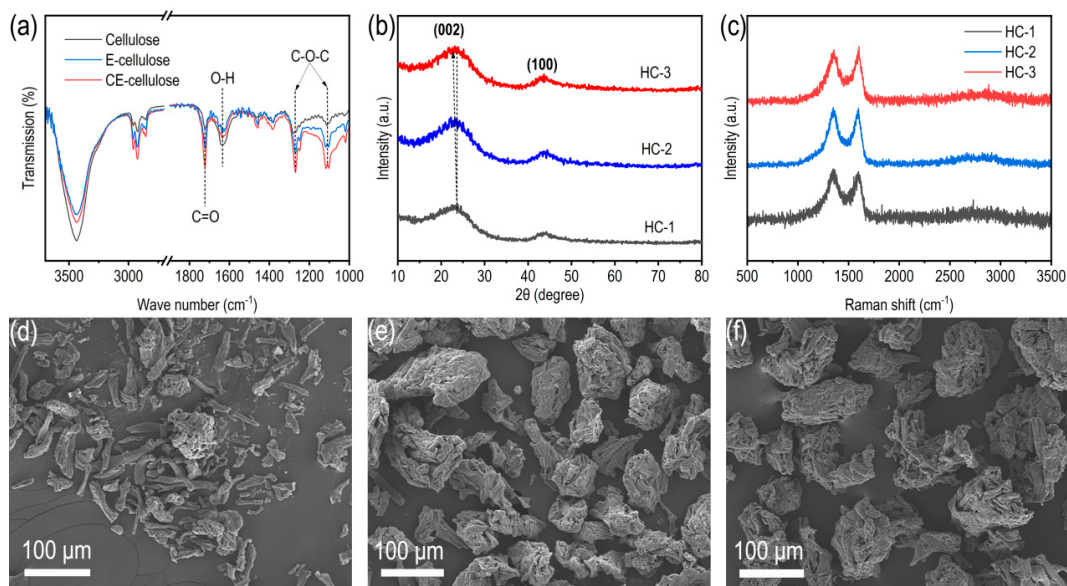


Figure 2. (a) FTIR spectra of cellulose, E-cellulose, and CE-cellulose. (b) XRD patterns and (c) Raman spectra of HC-1, HC-2, and HC-3. SEM images of (d) HC-1, (e) HC-2, and (f) HC-3.

To investigate the impact of ester grafting on the pyrolytic behavior of cellulose, thermogravimetric analysis (TG) was conducted under an argon atmosphere, spanning from room temperature to 1000 °C. The thermal decomposition temperature of cellulose, as depicted in Figure S1, exhibits a pronounced disparity compared to that of E-cellulose and CE-cellulose, suggesting distinct structural transformations occurring at the same temperature. The weight-loss rates of E-cellulose and CE-cellulose are significantly lower than that of cellulose, indicating a substantial improvement in the carbon yields (29% and 20% for CE-cellulose and E-cellulose, respectively) compared to that of cellulose (13%). This observation suggests that modifying the molecular structure of cellulose by esterification crosslinking not only alters the pyrolysis yield of cellulose, but also significantly influences the formation of carbon structures during the pyrolysis process.

To comprehensively characterize the structural attributes of hard carbons derived from cellulose with varying degrees of crosslinking, we conducted a series of analyses to elucidate their structural characteristics. Figure 2b illustrates the X-ray diffraction (XRD) patterns of

various hard carbon materials. From the figure, it is evident that all hard carbon samples exhibit two broad peaks at approximately 22° and 43° , corresponding to the (002) and (100) crystal planes, respectively, which indicate typical disordered structural characteristics. Notably, an increase in cellulose crosslinking leads to a discernible shift towards lower diffraction angles for the peak associated with the (002) crystal plane, implying alterations in interplanar spacing. According to the Bragg equation, which states that $2d\sin\theta = n\lambda$, we calculated the interlayer spacing of hard carbon samples. In this equation, θ represents the X-ray diffraction angle, λ is the wavelength of X-rays, and n is a periodic multiple of the wavelength (taking $n = 1$ in this case). By utilizing this equation to determine the center position of the (002) peak, we obtained d_{002} values for three types of hard carbon samples HC-1, HC-2, and HC-3 as 0.3757 nm, 0.3798 nm, and 0.3864 nm respectively, indicating that an increase in surface crosslinking of cellulose promotes expansion in the interlayer spacing of hard carbon.

The Raman spectra of three types of hard carbon materials are presented in Figure 2c. All samples exhibit characteristic peaks for hard carbon materials, namely a D peak at approximately 1350 cm^{-1} and a G peak at around 1580 cm^{-1} . The D peak is attributed to sp^3 hybridization of carbon atoms, while the G peak arises from stretching vibrations of sp^2 hybridized atomic pairs, representing the ordered and disordered structures of hard carbon materials, respectively. By calculating the ratio between the integrated areas under the D and G peaks, ID/IG values were determined as 1.96, 1.89, and 1.83 for HC-1, HC-2, and HC-3, respectively. These reduced ID/IG values indicate that the increase in cellulose crosslinking reduces the number of internal defects in hard carbon materials and improves their graphitization, which is consistent with the XRD analysis results.

The scanning electron microscopy (SEM) images of HC-1, HC-2, and HC-3 are presented in Figure 2d–f, respectively, elucidating the morphological alterations observed in hard carbon materials derived from cellulose through distinct pretreatment methodologies. The morphology of HC-1 mainly manifests as dispersed rod-shaped particles obtained from cellulose pyrolysis. As for HC-2 and HC-3, the predominant morphology is secondary particles consisting of rod-shaped units, which are derived from the aggregation of cellulose rods caused by the esterification between terephthalic acid and cellulose. The utilization of high-resolution transmission electron microscopy (TEM) further elucidates the alterations in crystal structure observed in various cross-linked cellulose-derived carbon materials. As depicted in Figure 3, HC-1 exhibits a classical porous architecture characterized by short-range order and long-range disorder, whereas HC-2 and HC-3 display a dense block consisting of carbon layer structures with more pronounced curves compared to HC-1, featuring well-defined closed pore structures.

The specific surface areas and pore structures of hard carbon materials were comprehensively characterized through nitrogen adsorption–desorption tests. Figure 4a illustrates the physical adsorption characteristics of three hard carbon materials (HC-1, HC-2, and HC-3). All samples exhibited characteristic Type IV adsorption isotherms. Based on BET model calculations, the specific surface areas of HC-1, HC-2, and HC-3 were determined to be $12.54\text{ m}^2\text{ g}^{-1}$, $6.078\text{ m}^2\text{ g}^{-1}$, and $4.663\text{ m}^2\text{ g}^{-1}$ respectively. Analysis of Figure 4b revealed that the hard carbon material possesses predominantly mesopores, with the average pore sizes measuring at 5.832 nm, 25.424 nm, and 20.055 nm correspondingly. These findings indicate that the incorporation of terephthalic acid into the precursor material leads to a significant decrease in specific surface area and an increase in pore size. This not only minimizes the formation of solid-electrolyte interphase (SEI) film, thereby enhancing the initial coulombic efficiency, but also promotes electrolyte infiltration and improves the rate performance of sodium storage.

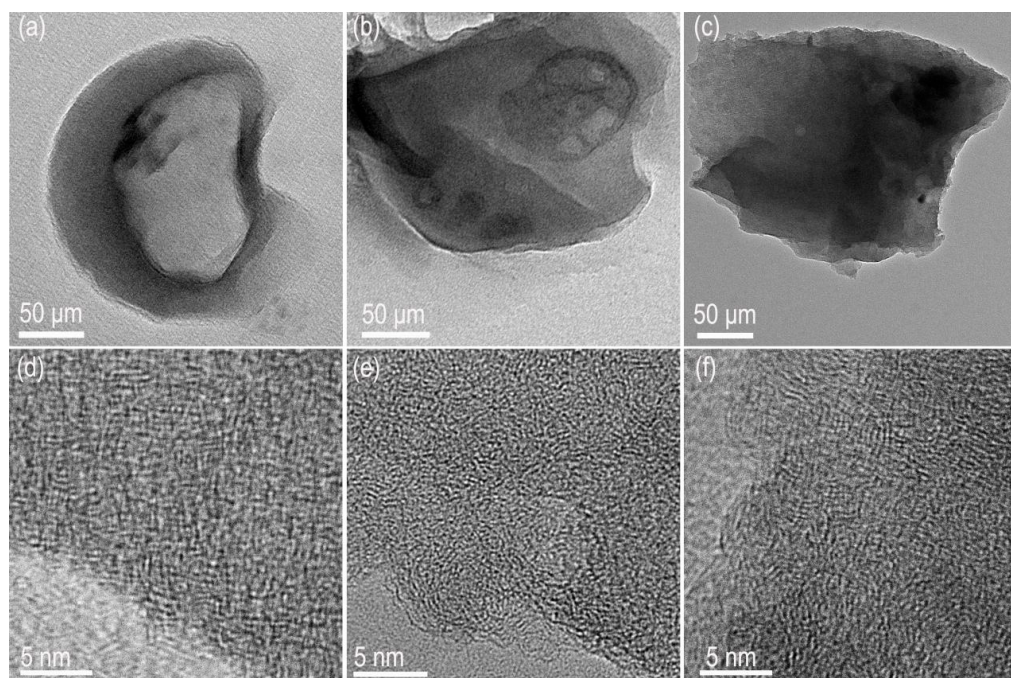


Figure 3. TEM images of (a) HC-1, (b) HC-2 and (c) HC-3. HRTEM images of (d) HC-1, (e) HC-2 and (f) HC-3.

The closed pore structure plays a crucial role in determining the performance of hard carbon for sodium storage. True density and small angle X-ray scattering (SAXS) are the primary techniques employed to assess the volume of closed pore structures. As displayed in Figure 4c, the true densities of HC-1, HC-2 and HC-3, as measured by the gas displacement method, are 2.37 g cm^{-3} , 2.33 g cm^{-3} , and 2.09 g cm^{-3} , respectively. These results for true density indicate that the closed pore volumes of esterification cross-linked cellulose pyrolysis hard carbon (HC-2 and HC-3) surpass that of cellulose pyrolysis hard carbon (HC-1). Moreover, a direct correlation is observed between the degree of esterification cross-linking of cellulose and the closed-pore volume of its pyrolysis hard carbon. Therefore, we conducted additional SAXS tests on the aforementioned samples to acquire pertinent insights into the enclosed pore structures. In SAXS spectra (Figure 4d), Q represents the scattering vector and is inversely proportional to the characteristic structure sizes (e.g., pores or particles) in the intensity of scattered X-rays. The lowest Q-value corresponds to the scattering on the surface of the particles, which is primarily attributed to the larger macroscopic surface area of hard carbon materials. In the intermediate Q-value range (around 0.1 \AA^{-1}), the intensity evolution exhibits a plateau followed by a downward inflection point, which is indicative of closed pores. Figure 4d demonstrates that HC-3 displays the highest scattering intensity and forms a distinct plateau at 0.1 \AA^{-1} . In contrast, HC-1 and HC-2 do not exhibit similar plateaus but rather show noticeable turning points. The test results suggest that HC-3 possesses more closed pore structures.

X-ray atomic pair distribution function (PDF) patterns have also been utilized to investigate the micro-nano structure of the prepared hard carbon samples. From a comparison of the X-ray PDF patterns of three samples in Figure 4e, it is evident that HC-1 exhibits the most rapid decay in the pairwise C-C correlations, indicating that it has the smallest domain sizes (ordered carbon-sheet structure) and a more disordered local structure. HC-3 exhibits the most stable pairwise C-C correlations, indicating that it has the largest domain sizes. More details of the pairwise C-C correlations of three samples are displayed in Figure 4f; it can be observed that HC-2 and HC-3 exhibit significant long-range pairwise C-C correlation offsets compared to HC-1, indicating a higher degree of curvature in the

domain sizes. This supports the SAXS findings that hard carbon derived from cellulose modified by esterification cross-linking has more closed pores.

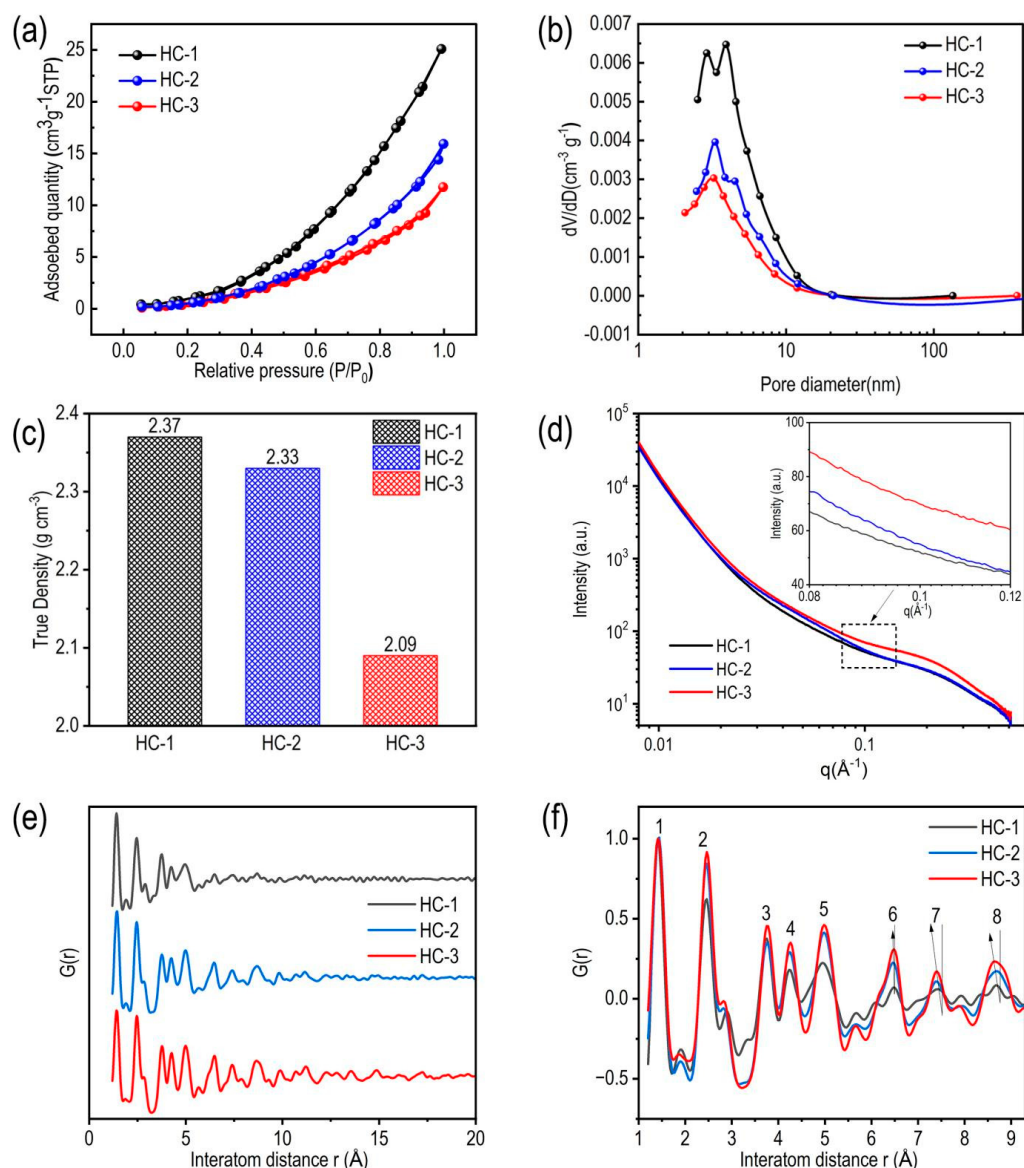


Figure 4. (a) Nitrogen adsorption–desorption isotherms, (b) pore size distributions, (c) true density, (d) SAXS patterns, (e,f) PDF patterns of HC-1, HC-2, and HC-3.

The electrochemical performances of HC-1, HC-2, and HC-3 were assessed through cyclic voltammetry (CV) and galvanostatic charge–discharge (GCD), employing a half-cell configuration with Na-metal as the reference electrode. As depicted in Figure 5a, the CV curves recorded the sodium storage characteristics of HC-1, HC-2, and HC-3 at a scanning rate of 0.1 mV s^{-1} . Near a low voltage of 0.1 V , a pair of distinct anodic Na^+ insertion peaks and cathodic Na^+ extraction peaks were observed, indicating the occurrence of sodium ion insertion and extraction processes within the pseudo-graphite layer of hard carbon, contributing to a portion of its plateau capacity. Additionally, as illustrated in the inset figure within Figure 5a and Figure S2, HC-1, HC-2, and HC-3 exhibit peak potentials for Na^+ extraction at 0.206 V , 0.198 V , and 0.168 V , respectively. This suggests that a reduction in the polarization potential for Na^+ insertion and extraction is correlated with the increase in closed-pore volume in hard carbon, which significantly improved the kinetics of Na^+ insertion and extraction. Figure 5b shows the galvanostatic charge–discharge (GCD)

tests for the hard carbon materials (HC-1, HC-2, HC-3) at a current density of 5 mA g^{-1} . According to the test results, HC-1, HC-2, and HC-3 exhibited reversible capacities of 254.3 mAh g^{-1} , $312.68 \text{ mAh g}^{-1}$, and $347.77 \text{ mAh g}^{-1}$, respectively, with initial coulombic efficiencies of 77.3%, 76.5%, and 85.6%. Moreover, the charge–discharge curves of HC-1, HC-2 and HC-3 exhibited two distinct regions: a sloping region with voltage greater than 0.1 V and a plateau region with voltage less than 0.1 V. Previous research has revealed that different curve regions correspond to different mechanisms of sodium ion storage: (1) the sloping region is closely linked to adsorption of sodium ions on the surface and defects of hard carbon; (2) the plateau region has obvious relevance to insertion reactions of sodium ions within pseudo-graphite layers and filling reactions of sodium ions within closed nanopores. To further investigate the disparities in sodium storage performance among the three hard carbon samples, the reversible capacities of HC-1, HC-2 and HC-3 were decomposed into two components, sloping capacity and plateau capacity, in order to conduct a comprehensive analysis. As depicted in Figure 5c, the sloping capacities for HC-1, HC-2, and HC-3 are 114.5 mAh g^{-1} , 112 mAh g^{-1} , and 118 mAh g^{-1} , respectively, with relatively minor variations. Conversely, the plateau capacity demonstrates a significant increase from 140 mAh g^{-1} to 201 mAh g^{-1} for HC-2 and further to 230 mAh g^{-1} for HC-3. The proportions of plateau capacity for HC-1, HC-2 and HC-3 are 55.1%, 64.2% and 66.1%, respectively. After a comparison of the aforementioned data, it can be confidently concluded that the increase in the crosslinking of cellulose leads to enhancements in the reversible capacity of the corresponding hard carbon, which can be primarily attributed to the augmentation of plateau capacity. Moreover, Figure S3 and the inset figure within Figure 5b illustrate not only that the plateau capacities of HC-2 and HC-3 surpass that of HC-1, but also that these materials exhibit significantly lower charging midpoint voltages compared to HC-1.

Rate performance tests of HC-1, HC-2, and HC-3 were further carried out at a galvanostatic discharge current density of 0.01 A g^{-1} and multiple charge current densities ($0.01, 0.02, 0.05, 0.1, 0.2, 0.5$, and 1 A g^{-1}). Compared with HC-2 and HC-3, the specific capacity of HC-1 exhibited a significant capacity decline with increasing current density, as illustrated in Figure 5d. At a current density of 1 A g^{-1} , the capacity of HC-1 was measured to be 218.6 mAhg^{-1} , demonstrating a capacity retention of 88.2%. In contrast, HC-2 and HC-3 displayed capacities of 282.2 mAhg^{-1} and 317.2 mAhg^{-1} , respectively, resulting in higher capacity retentions: 94.1% and 96.3%. Figure 5e demonstrates the cycle stability of HC-1, HC-2, and HC-3 at a current density of 20 mA g^{-1} . The initial specific capacities of HC-1, HC-2 and HC-3 were 331, 301, and 250 mAh g^{-1} , respectively. However, after 500 cycles, the specific capacity of HC-1 dropped to 162 mAh g^{-1} , resulting in a capacity retention of about 65%. On the other hand, after 500 cycles, the specific capacities of HC-2 and HC-3 were 256 mAh g^{-1} and 293 mAh g^{-1} , with capacity retentions of 85% and 88%, respectively. This result implies that the increase in the quantity of closed pores in hard carbon enhances the sodium storage capacity, kinetics, and cycle stability.

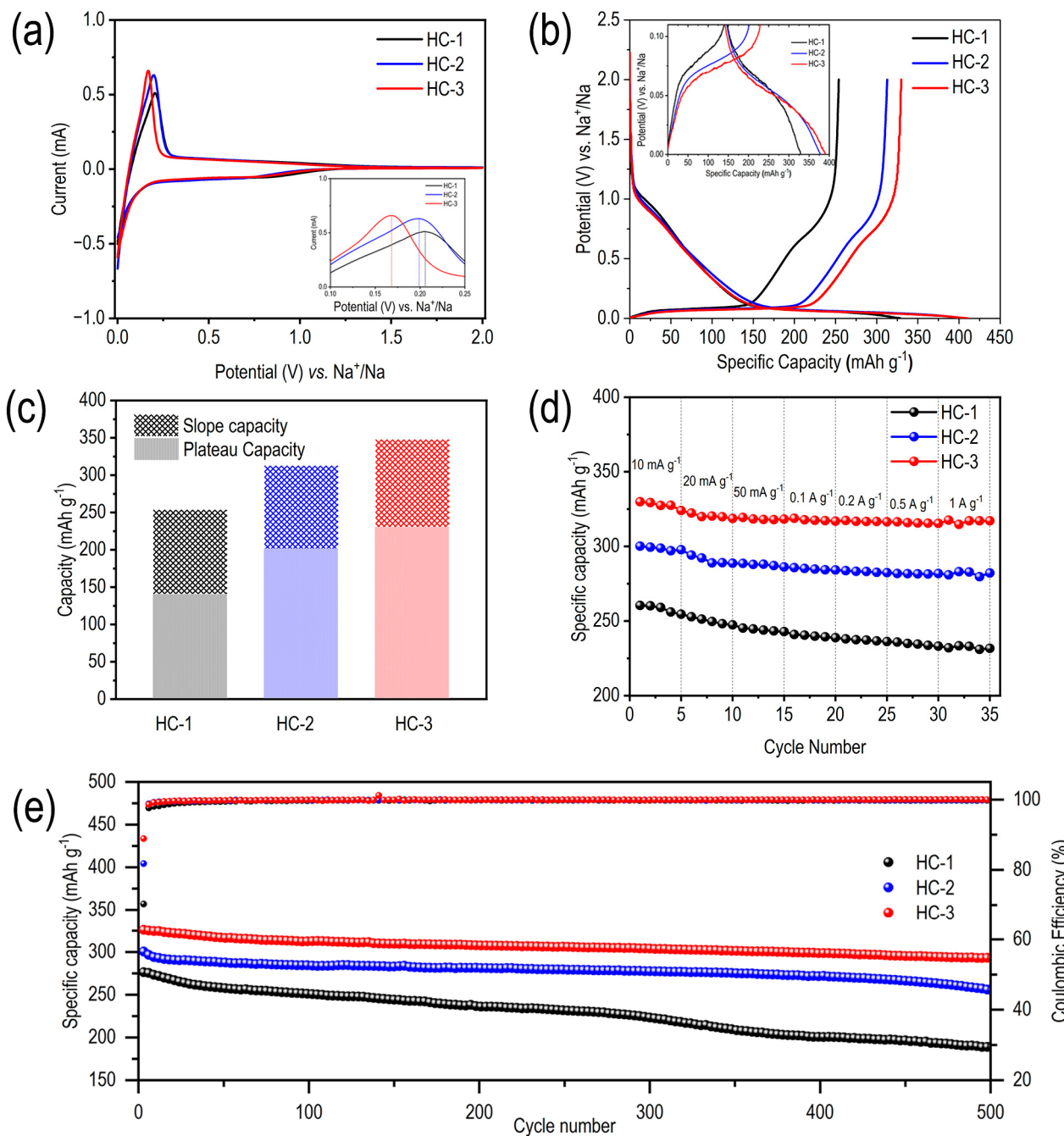


Figure 5. The electrochemical performances of HC-1, HC-2, and HC-3. **(a)** The first CV curves at 0.1 mV s^{-1} , **(b)** the initial galvanostatic charge–discharge profiles, **(c)** the capacity segmentation, **(d)** the rate performance, and **(e)** the cycle stability.

4. Conclusions

In this paper, by employing esterification crosslinking to modify the surface molecular structure of cellulose, we successfully synthesized a diverse range of surface-modified celluloses and generated nano-structural modified hard carbons through carbonization. By conducting a comparative analysis of the structures of diverse cross-linked precursor hard carbons, we observed that an increase in the degree of crosslinking in cellulose leads to enhanced carbon-layer development and an increased quantity of closed pores in hard carbon materials, along with a significant reduction in specific surface area. By optimizing the esterification cross-linking modification, we have successfully enhanced the sodium storage capacity of cellulose-derived hard carbon from 254 mAh g^{-1} to 348 mAh g^{-1} and achieved an

applicable initial coulomb efficiency (ICE) exceeding 85%, surpassing the performance of currently available commercialized hard carbon products. In conjunction with the low cost of cellulose and the scalable nature of the process for industrialization, this breakthrough demonstrates significant potential for industrial application.

Supplementary Materials: The following supporting information can be downloaded at: <https://www.mdpi.com/article/10.3390/batteries11010036/s1>, Figure S1: TG curves of cellulose, E-cellulose and CE-cellulose; Figure S2: the Na^+ extraction peaks of HC-1, HC-2 and HC-3 in the CV curves; Figure S3: the plateau capacity of HC-1, HC-2 and HC-3; Table S1: Comparison of Sodium Storage Performance among Various Types of Hard Carbon.

Author Contributions: Conceptualization, J.L. and S.S.; methodology, Y.W.; validation, Y.H.; formal analysis, X.Z. and Y.H.; investigation, X.Z. and Y.H.; resources, M.L. and C.L.; data curation, Y.H.; writing—original draft preparation, X.Z. and Y.H.; writing—review and editing, X.Z. and Y.H. All authors have read and agreed to the published version of the manuscript.

Funding: This work was funded by the Taishan Scholars Program (NO. tsqnz20230629); the Western Young Scholars Foundations of Chinese Academy of Sciences; the National Natural Science Foundation of China (Grant Nos. 52102249), the Science Fund of Shandong Laboratory of Yantai Advanced Materials and Green Manufacturing [AMGM2022A02, AMGM2023A04]; the Collaborative Innovation Alliance Fund for Young Science and Technology Worker (HZJJ23-5).

Data Availability Statement: The original contributions presented in the study are included in the article, further inquiries can be directed to the corresponding author.

Acknowledgments: This work was supported by Shandong Laboratory of Advanced Materials and Green Manufacturing at Yantai.

Conflicts of Interest: The authors declare no conflicts of interest.

References

1. Che, C.; Wu, F.; Li, Y.; Li, S.; Wu, C.; Bai, Y. Challenges and Breakthroughs in Enhancing Temperature Tolerance of Sodium-Ion Batteries. *Adv. Mater.* **2024**, *36*, 2402291. [[CrossRef](#)] [[PubMed](#)]
2. Cheng, F.Y.; Zhang, W.; Qin, D.M.; Sun, S.X.; Xu, Y.; Li, Q.; Fang, C.; Han, J.T.; Huang, Y.H. Reinterpreting the correlation between cycling stability of Ni-rich layered oxide cathode and the charging cut-off voltage in Li-ion batteries. *Nano Energy* **2023**, *115*, 108699. [[CrossRef](#)]
3. Duffner, F.; Kronemeyer, N.; Tuebke, J.; Leker, J.; Winter, M.; Schmuck, R. Post-lithium-ion battery cell production and its compatibility with lithium-ion cell production infrastructure. *Nat. Energy* **2021**, *6*, 123–134. [[CrossRef](#)]
4. Gao, Y.; Pan, Z.; Sun, J.; Liu, Z.; Wang, J. High-Energy Batteries: Beyond Lithium-Ion and Their Long Road to Commercialisation. *Nano-Micro Lett.* **2022**, *14*, 94. [[CrossRef](#)]
5. Zhang, M.; Li, Y.; Wu, F.; Bai, Y.; Wu, C. Boost sodium-ion batteries to commercialization: Strategies to enhance initial Coulombic efficiency of hard carbon anode. *Nano Energy* **2021**, *82*, 105738. [[CrossRef](#)]
6. Chen, D.; Zhang, W.; Luo, K.; Song, Y.; Zhong, Y.; Liu, Y.; Wang, G.; Zhong, B.; Wu, Z.; Guo, X. Hard carbon for sodium storage: Mechanism and optimization strategies toward commercialization. *Energy Environ. Sci.* **2021**, *14*, 2244–2262. [[CrossRef](#)]
7. Chu, Y.; Zhang, J.; Zhang, Y.; Li, Q.; Jia, Y.; Dong, X.; Xiao, J.; Tao, Y.; Yang, Q.-H. Reconfiguring Hard Carbons with Emerging Sodium-Ion Batteries: A Perspective. *Adv. Mater.* **2023**, *35*, 2212186. [[CrossRef](#)]
8. Guo, Z.; Qian, G.; Wang, C.; Zhang, G.; Yin, R.; Liu, W.-D.; Liu, R.; Chen, Y. Progress in electrode materials for the industrialization of sodium-ion batteries. *Prog. Nat. Sci. Mater.* **2023**, *33*, 1–7. [[CrossRef](#)]
9. Ma, S.; Yan, W.; Dong, Y.; Su, Y.; Ma, L.; Li, Y.; Fang, Y.; Wang, B.; Wu, S.; Liu, C.; et al. Recent advances in carbon-based anodes for high-performance sodium-ion batteries: Mechanism, modification and characterizations. *Mater. Today* **2024**, *75*, 334–358. [[CrossRef](#)]
10. Wang, T.; Shi, Z.; Zhong, Y.; Ma, Y.; He, J.; Zhu, Z.; Cheng, X.-B.; Lu, B.; Wu, Y. Biomass-Derived Materials for Advanced Rechargeable Batteries. *Small* **2024**, *20*, 2310907. [[CrossRef](#)]
11. Liu, L.; Xu, Q.; Yin, S.; Liu, Z.; Li, Y.; Pang, W. Recent progress on hard carbon-based anode for sodium-ion battery. *J. Power Sources* **2024**, *615*, 235116. [[CrossRef](#)]

12. Lin, J.; Zhou, Q.; Liao, Z.; Chen, Y.; Liu, Y.; Liu, Q.; Xiong, X. Steric Hindrance Engineering to Modulate the Closed Pores Formation of Polymer-Derived Hard Carbon for High-Performance Sodium-Ion Batteries. *Angew. Chem. (Int. Ed. Engl.)* **2024**, *63*, e202409906.
13. Guo, L.; Huang, M.; Liu, W.; Zhu, H.; Cheng, Y.; Wang, M.-S. Pore-size tuning of hard carbon to optimize its wettability for efficient Na^+ storage. *J. Mater. Chem. A* **2024**, *12*, 13703–13712. [[CrossRef](#)]
14. Hu, Q.; Xu, L.; Liu, G.; Hu, J.; Ji, X.; Wu, Y. Understanding the Sodium Storage Behavior of Closed Pores/Carbonyl Groups in Hard Carbon. *ACS Nano* **2024**, *18*, 21491–21503. [[CrossRef](#)]
15. Zhao, X.; Shi, P.; Wang, H.; Meng, Q.; Qi, X.; Ai, G.; Xie, F.; Rong, X.; Xiong, Y.; Lu, Y.; et al. Unlocking plateau capacity with versatile precursor crosslinking for carbon anodes in Na-ion batteries. *Energy Storage Mater.* **2024**, *70*, 103543. [[CrossRef](#)]
16. Zhou, H.; Song, Y.; Zhang, B.; Sun, H.; Khurshid, I.A.; Kong, Y.; Chen, L.; Cui, L.; Zhang, D.; Wang, W.; et al. Overview of electrochemical competing process of sodium storage and metal plating in hard carbon anode of sodium ion battery. *Energy Storage Mater.* **2024**, *71*, 103645. [[CrossRef](#)]
17. Li, X.; Zhang, S.; Tang, J.; Yang, J.; Wen, K.; Wang, J.; Wang, P.; Zhou, X.; Zhang, Y. Structural design of biomass-derived hard carbon anode materials for superior sodium storage via increasing crystalline cellulose and closing the open pores. *J. Mater. Chem. A* **2024**, *12*, 21176–21189. [[CrossRef](#)]
18. Kong, X.; Qin, H.; Li, X.; Guo, L.; Chen, Y. Self-activation strategy-synthesized hierarchical micro-mesoporous hard carbon with superior sodium ions storage. *J. Mater. Sci.* **2024**, *59*, 13602–13613. [[CrossRef](#)]
19. Guo, L.; Qiu, C.; Yuan, R.; Li, X.; Li, X.; Li, K.; Zhu, W.; Liu, X.; Li, A.; Liu, H.; et al. Boosting Molecular Cross-Linking in a Phenolic Resin for Spherical Hard Carbon with Enriched Closed Pores toward Enhanced Sodium Storage Ability. *ACS Appl. Mater. Interfaces* **2024**, *16*, 27419–27428. [[CrossRef](#)]
20. Aina, S.; Tratnik, B.; Vizintin, A.; Tchernychova, E.; Lobera, M.P.; Dominko, R.; Bernechea, M. Simple surface treatment improves performance of carbon materials for sodium ion battery anodes. *J. Power Sources* **2024**, *610*, 234730. [[CrossRef](#)]
21. Rajh, A.; Gabrijelcic, M.; Tratnik, B.; Bucar, K.; Arcon, I.; Petric, M.; Dominko, R.; Vizintin, A.; Kavcic, M. Structural and chemical analysis of hard carbon negative electrode for Na-ion battery with X-ray Raman scattering and solid-state NMR spectroscopy. *Carbon* **2024**, *228*, 119398. [[CrossRef](#)]
22. Ruetzler, A.; Buettner, J.; Oechsler, J.; Balaghi, S.E.; Kuespert, S.; Ortlieb, N.; Fischer, A. Mesoporous N-Doped Carbon Nanospheres as Anode Material for Sodium Ion Batteries with High Rate Capability and Superior Power Densities. *Adv. Funct. Mater.* **2024**, *34*, 2401188. [[CrossRef](#)]
23. Qiao, S.; Zhou, Q.; Ma, M.; Liu, H.K.; Dou, S.X.; Chong, S. Advanced Anode Materials for Rechargeable Sodium-Ion Batteries. *ACS Nano* **2023**, *17*, 11220–11252. [[CrossRef](#)]
24. He, Y.; Liu, D.; Jiao, J.; Liu, Y.; He, S.; Zhang, Y.; Cheng, Q.; Fang, Y.; Mo, X.; Pan, H.; et al. Pyridinic N-Dominated Hard Carbon with Accessible Carbonyl Groups Enabling 98% Initial Coulombic Efficiency for Sodium-Ion Batteries. *Adv. Funct. Mater.* **2024**, *34*, 2403144. [[CrossRef](#)]
25. Song, Z.; Di, M.; Zhang, X.; Wang, Z.; Chen, S.; Zhang, Q.; Bai, Y. Nanoconfined Strategy Optimizing Hard Carbon for Robust Sodium Storage. *Adv. Energy Mater.* **2024**, *14*, 2401763. [[CrossRef](#)]
26. Sun, D.; Zhao, L.; Sun, P.; Zhao, K.; Sun, Y.; Zhang, Q.; Li, Z.; Ma, Z.; Zheng, F.; Yang, Y.; et al. Rationally Regulating Closed Pore Structures by Pitch Coating to Boost Sodium Storage Performance of Hard Carbon in Low-voltage Platforms. *Adv. Funct. Mater.* **2024**, *34*, 2403642. [[CrossRef](#)]

Disclaimer/Publisher’s Note: The statements, opinions and data contained in all publications are solely those of the individual author(s) and contributor(s) and not of MDPI and/or the editor(s). MDPI and/or the editor(s) disclaim responsibility for any injury to people or property resulting from any ideas, methods, instructions or products referred to in the content.